



RESEARCH ARTICLE

10.1029/2023JD039489

Process Modeling of Aerosol-Cloud Interaction in Summertime Precipitating Shallow Cumulus Over the Western North Atlantic

Key Points:

- Aerosol-cloud interactions in precipitating shallow cumuli are investigated using large-eddy simulations (LES) and observations
- LES show that aerosol-induced cumulus cloud water adjustment is dominated by precipitation with no clear entrainment feedback
- An increase in cloud fraction in response to aerosol number concentration decrease is shown in the precipitating cumuli

Supporting Information:

Supporting Information may be found in the online version of this article.






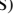














Correspondence to:

X.-Y. Li and H. Wang,
xiangyu.li@pnnl.gov;
hailong.wang@pnnl.gov

Citation:

Li, X.-Y., Wang, H., Christensen, M. W., Chen, J., Tang, S., Kirschler, S., et al. (2024). Process modeling of aerosol-cloud interaction in summertime precipitating shallow cumulus over the Western North Atlantic. *Journal of Geophysical Research: Atmospheres*, 129, e2023JD039489. <https://doi.org/10.1029/2023JD039489>

Received 20 JUN 2023
Accepted 7 MAR 2024

Xiang-Yu Li¹ , Hailong Wang¹ , Matthew W. Christensen¹ , Jingyi Chen¹ , Shuaiqi Tang¹ , Simon Kirschler² , Ewan Crosbie^{3,4} , Luke D. Ziemba³ , David Painemal^{3,4}, Andrea F. Corral⁵, Kayla Ann McCauley⁶, Sanja Dmitrovic⁷, Armin Sorooshian^{5,6}, Marta Fenn^{3,8} , Joseph S. Schlosser^{3,9} , Snorre Stamnes³, Johnathan W. Hair³ , Brian Cairns¹⁰, Richard Moore³ , Richard Anthony Ferrare³ , Michael A. Shook³ , Yonghoon Choi^{3,4} , Glenn S. Diskin³ , Joshua DiGangi³ , John B. Nowak³ , Claire Robinson^{3,4}, Taylor J. Shingler³, Kenneth Lee Thornhill³ , and Christiane Voigt² 

¹Pacific Northwest National Laboratory, Richland, WA, USA, ²Institut für Physik der Atmosphäre, Deutsches Zentrum für Luft- und Raumfahrt (DLR), and Institute for Physics of the Atmosphere, Johannes Gutenberg-University Mainz, Mainz, Germany, ³NASA Langley Research Center, Hampton, VA, USA, ⁴Analytical Mechanics Associates, Hampton, VA, USA, ⁵Department of Chemical and Environmental Engineering, University of Arizona, Tucson, AZ, USA, ⁶Department of Hydrology and Atmospheric Sciences, University of Arizona, Tucson, AZ, USA, ⁷University of Arizona, James C. Wyant College of Optical Sciences, Tucson, AZ, USA, ⁸Coherent Applications, Inc., Hampton, VA, USA, ⁹NASA Postdoctoral Program, NASA Langley Research Center, Hampton, VA, USA, ¹⁰NASA Goddard Institute for Space Studies, New York, NY, USA

Abstract Process modeling of Aerosol-cloud interaction (ACI) is essential to bridging gaps between observational analysis and climate modeling of aerosol effects in the Earth system and eventually reducing climate projection uncertainties. In this study, we examine ACI in summertime precipitating shallow cumuli observed during the Aerosol Cloud meteorology Interactions over the western Atlantic Experiment (ACTIVATE). Aerosols and precipitating shallow cumuli were extensively observed with in-situ and remote-sensing instruments during two research flight cases on 02 June and 07 June, respectively, during the ACTIVATE summer 2021 deployment phase. We perform observational analysis and large-eddy simulation (LES) of aerosol effect on precipitating cumulus in these two cases. Given the measured aerosol size distributions and meteorological conditions, LES is able to reproduce the observed cloud properties by aircraft such as liquid water content (LWC), cloud droplet number concentration (N_c) and effective radius r_{eff} . However, it produces smaller liquid water path (LWP) and larger N_c compared to the satellite retrievals. Both 02 and 07 June cases are over warm waters of the Gulf Stream and have a cloud top height over 3 km, but the 07 June case is more polluted and has larger LWC. We find that the N_a -induced LWP adjustment is dominated by precipitation feedback for the 2 June precipitating case and there is no clear entrainment feedback in both cases. An increase of cloud fraction due to a decrease of aerosol number concentration is also shown in the simulations for the 02 June case.

Plain Language Summary Aerosol-cloud-interaction (ACI) regulates the energy budget of the Earth and poses the largest uncertainty in climate projection. Particularly, ACI of low clouds is poorly understood and causes the spread of Earth System Models (ESMs) in predicting cloud and climate responses to aerosol changes. Process studies have shown a nonlinear cloud water amount and cloud fraction adjustments due to aerosol changes via precipitation and cloud top entrainment, which are not often captured correctly in ESMs. This study explores the physical mechanisms of ACI in marine low clouds with a focus on precipitating low clouds using a cloud process model and unprecedented field campaign measurements of meteorology states, cloud properties, and aerosols collected during the Aerosol Cloud meteorology Interactions over the western Atlantic Experiment. We show that the aerosol-induced cloud water amount adjustment is dominated by changes in precipitation and there is no clear entrainment feedback in both cases. Our findings can help improve the representation of ACI within precipitating marine low clouds in ESMs.

1. Introduction

Aerosol-cloud interaction (ACI) poses the largest uncertainty for accurate climate projection (Seinfeld et al., 2016). Assuming fixed Liquid Water Path (LWP) and Cloud Fractional Coverage (CFC), increasing the

© 2024 Battelle Memorial Institute and The Authors. This article has been contributed to by U.S. Government employees and their work is in the public domain in the USA. This is an open access article under the terms of the [Creative Commons Attribution-NonCommercial-NoDerivs License](https://creativecommons.org/licenses/by-nc-nd/4.0/), which permits use and distribution in any medium, provided the original work is properly cited, the use is non-commercial and no modifications or adaptations are made.

aerosol number concentration N_a leads to a larger cloud droplet number concentration N_c , smaller effective radius r_{eff} , and stronger outgoing shortwave (SW) radiation (Twomey, 1977). The enhanced SW cloud radiative effect can affect the meteorological state and boundary layer structure of clouds (X.-Y. Li et al., 2023). Decreased r_{eff} suppresses the precipitation rate by inhibiting the collision-coalescence processes, resulting in a higher LWP and possibly larger CFC (Albrecht, 1989). This is the conventional wisdom of ACI involving multi-scale, nonlinear processes from aerosol and cloud microphysics to large-scale atmospheric circulations, which are fundamentally poorly understood due to the intractable scale range and strong nonlinearity, and therefore, mathematically poorly represented in Earth System Models (ESMs) (Seinfeld et al., 2016; Smith et al., 2020). Besides the strongly nonlinear nature of ACI, it is also in an emergent and non-equilibrium state, which hinders our understanding of processes that determines sinks and sources of aerosol and cloud. One example is the nonlinear interplay among N_a , N_c , and the sink terms of liquid water content (LWC) for summertime shallow cumuli (Seinfeld et al., 2016). The parameterization of these clouds is responsible for the spread of ESMs in estimating the equilibrium climate sensitivity (ECS) (Zhao et al., 2016). In addition, even though ACI of shallow cumuli was shown to affect the ECS (Gettelman et al., 2019), the magnitude is uncertain. Droplet evaporation and precipitation are the two major sinks of LWC. Larger N_a results in larger N_c but smaller cloud droplets, which are easier to evaporate. N_a -induced suppression of the precipitation rate leads to a positive LWP response (Glassmeier et al., 2021). Precipitation removes aerosols from clouds and therefore leads to a negative feedback on N_c (Radke et al., 1980). This LWP feedback is also influenced by aerosol hygroscopicity (κ), which determines the activation rate of aerosols acting as cloud condensation nuclei (CCN) to form cloud droplets. κ poses a great challenge for ESMs due to uncertainties in the detailed composition of particles, aerosol mixing state, and potential nonlinear interactions between them (Petters & Kreidenweis, 2007).

The aforementioned aerosol-cloud-precipitation interaction is very challenging to simulate even using large-eddy simulations (LES), where the relevant large-size turbulent eddies for cloud formation are resolved but droplet-turbulence interactions are ignored. The latter (X.-Y. Li et al., 2020) enhances the collision-coalescence process that determines the precipitation rate. Ackerman et al. (2004) showed that LWP response to aerosol-induced precipitation suppression depends on the competition between moistening due to decreased surface precipitation and drying due to enhanced cloud top entrainment. Therefore, the LWP adjustment in response to increasing N_a can be divided into entrainment-dominated and precipitation-dominated regimes. For non-precipitating stratocumuli (typically having the appearance of closed cells), increasing N_a leads to more abundant, smaller cloud droplets that can evaporate more readily due to entrainment drying because smaller droplets provide a larger surface area for a fixed amount of LWP (Ackerman et al., 2004). This entrainment drying feedback leads to a negative LWP adjustment to increasing N_a , indicating less reflective clouds and therefore, a weaker cooling effect. For precipitating clouds (typically having the appearance of open cells), more abundant but smaller cloud droplets increase colloidal stability through the suppression of precipitation rate, and thus yield a larger value of LWP. This positive LWP adjustment to increasing N_a indicates thicker and more reflective clouds, that is, a stronger SW radiative cooling effect (Albrecht, 1989). Satellite observations have suggested complex LWP adjustments. Gryspeerdt et al. (2019) showed a negative LWP adjustment in the majority of the oceanic regions using satellite retrievals, indicating that LWP reductions due to ACI could offset a significant fraction of the indirect aerosol radiative effect related to albedo increase. Diamond et al. (2020) reported significant cloud brightening due to increased N_a from ship emissions in subtropical low clouds, which is refuted by Glassmeier et al. (2021), who pointed out that the shipping-induced aerosol radiative cooling for non-precipitating stratocumuli is overestimated by a factor of up to 200% because of the underestimated negative LWP adjustment related to current estimates of the average lifetimes of ship tracks. However, by considering both visible (as in Glassmeier et al., 2021) and invisible ship tracks, Manshausen et al. (2022) showed positive LWP adjustment and therefore, a larger aerosol cooling effect. Aerosol effects on LWP and CFC based on satellite measurements only use snapshots of aerosol-cloud fields and ignore the temporal nature of cloud adjustments, which could lead to inaccurate estimation of aerosol effects (Bellouin et al., 2020). Recently, Arola et al. (2022) found that a positive LWP adjustment can be easily misinterpreted as a negative adjustment based on satellite measurements due to satellite retrieval errors (Painemal & Zuidema, 2011) and the propagation and spatial variability in aerosols and clouds that cannot be captured by satellite instruments. In addition, Christensen et al. (2022) concluded that these results from natural experiments cannot be easily scaled to global scales. This is because only shallow clouds are considered and the effect of emission on deeper clouds is omitted in natural experiments. Modeling studies (Possner et al., 2018; Wang et al., 2011) have shown that cloud brightening and LWP adjustments in response to aerosol emissions from ships depend strongly on boundary-layer meteorological conditions and dynamical

feedback induced by precipitation change. This drives the need for an in-depth investigation of ACI in a more comprehensive meteorological context. The Aerosol Cloud meTeorology Interactions oVer the western ATLantic Experiment (ACTIVATE) field campaign (2020–2022) has been conducted to bridge such a gap.

Many studies focus on stratocumulus-to-cumulus cloud transitions, of which the physical drivers and feedbacks are still unclear (Sandu & Stevens, 2011). Wang and Feingold (2009) showed that precipitation change can drive the transition. Yamaguchi et al. (2017) and Wood et al. (2018) found fast transition (~ 10 hr) because of the drizzle initiation and depletion of aerosols by precipitation change using LES. A larger N_a elongates the timing of the transition even though it is modulated by the diurnal cycle and large-scale meteorology, as shown in the LES studies (Goren et al., 2019). Using satellite retrievals, Christensen et al. (2020) showed that aerosols enhance the lifetime of clouds and increase CFC in stable atmospheric conditions during the stratocumulus-to-cumulus transition. Erfani et al. (2022) confirmed the delayed stratocumulus-to-cumulus-transition due to aerosol-cloud-precipitation interactions for initially clean MBL and Twomey effect for initially polluted MBL using LES with a prognostic aerosol model, where aerosol life cycle with sources and sinks of aerosols included. However, studies on ACI of the strongly non-stationary precipitating cumuli are scarce.

In this study, we consider precipitating summertime cumuli observed during ACTIVATE since they can rapidly form rain (Raubert et al., 2007) and are an ideal candidate to study aerosol-cloud-precipitation interactions. In addition, the CFC of these clouds are severely under-predicted (few percent) in the ESMs (Rémillard & Tselioudis, 2015; Sorooshian et al., 2019) compared to the satellite observations (15 – 20%) in the North Atlantic region. We investigate the ACI of summertime cumuli over the Western North Atlantic Ocean (WNAO) region using LES and measurements during the ACTIVATE campaign. The ACTIVATE campaign aims to build unprecedented statistics to improve process-level understanding of ACI and their representation in ESMs (Sorooshian et al., 2019). To study aerosol-cloud-precipitation interactions, we select two contrasting cases from the ACTIVATE campaign. The first one is a clean case with heavier precipitation. The second one is a polluted case with light drizzling conditions. Contrary to most previous process studies that focused on sensitivity tests of ACI by arbitrarily perturbing the N_a or N_c (Chen et al., 2011; Goren et al., 2019; Wang & Feingold, 2009; Yamaguchi et al., 2017), we utilize measured N_a and N_c from ACTIVATE to understand ACI and its impact on LWP and CFC adjustments.

2. Data and Methods

2.1. Observations and Reanalysis Data

2.1.1. Two Precipitating Cases

We select two contrasting process-study cases during the ACTIVATE 2021 summer field campaign. The case on 02 June 2021 is a precipitating case (see the satellite visible image in Figure S1a in Supporting Information S1) while the one on 07 June 2021 (Figure S1b in Supporting Information S1) is a drizzling case. Figure S2 in Supporting Information S1 shows the rain rate frequency derived from the fast cloud droplet probe (FCDP) and two-dimensional stereo (2DS) probe (integrated from droplets with diameter from 3 to 1,400 μm) for the full flight. The 02 June 2021 case (RF77, black dots) has higher rain rate frequency than the 07 June 2021 case (RF80, red pluses). In addition, the highest rain rate reaches 23 mm hr^{-1} for the 02 June 2021 case while it ends around 5 mm hr^{-1} for the 07 June 2021 case. Our categorization of the precipitation for these two cases is also supported by the Falcon forward camera records. Both cases feature cumuli. The cloud top height (CTH) reaches about 4 km for the 02 June 2021 case and 3.5 km for the 07 June 2021 case according to the High Spectral Resolution Lidar CTH measurement (Figures S3a and S3c in Supporting Information S1) from the high-flying aircraft and the maximum height of the above-cloud-top flight legs of the low-flying aircraft. In addition, the CTH exhibit strong spatiotemporal variations for both cases, as shown by the time series of HSRL-CTH and the corresponding frequency in Figure S3 in Supporting Information S1. The strong fluctuations of LWP are shown in Figures 4a and 8a for the 02 and 07 June cases, respectively. This makes it more challenging for LES to simulate these clouds than the well-defined cold-air outbreak clouds observed over the WNAO region. The ACTIVATE campaign employed a dual-aircraft strategy to provide spatially coordinated measurements of meteorology states, trace gases, aerosol, and cloud properties (Sorooshian et al., 2019, 2023). The high-flying (~ 9 km in altitude) King Air measures meteorology states using dropsonde (X.-Y. Li et al., 2022) as well as aerosol and cloud retrievals using remote sensing instruments. The low-flying Falcon conducts in-situ measurements of water vapor (Diskin et al., 2002), trace gases, aerosol, and cloud properties. Figures S4 and S5 in Supporting Information S1 shows the

Table 1
List of Simulations

Simulations	N_a^{input} [cm^{-3}]	$\bar{\kappa}$
0602_NA1	707	0.55
0602_NA2	425	0.53
0602_NA3	354	0.55
0607_NA1	2,073	0.35
0607_NA2	1,233	0.30
0607_NA3	4,146	0.35

Note. “NA” denotes prescribed N_a measured below cloud base. Aerosol size distributions derived from two BCB flight legs (NA1 and NA2) are used as input for each case. Simulation 0602_NA3 is the same as 0602_NA1 but with halved N_a^{input} . Simulation 0607_NA3 is the same as 0607_NA1 but with doubled N_a^{input} .

vertical profiles of water vapor mixing ratio q_v at 12 dropsonde locations and the simultaneously measured N_c from the FCDP for the 02 and 07 June 2021 cases, respectively. The measurements took place between 18:29:20 to 19:46:16 UTC and 18:25:54 to 19:45:37 UTC for the 02 and 07 June 2021 cases, respectively.

2.1.2. Measured Aerosol Size Distribution

A Scanning Mobility Particle Sizer (SMPS, TSI model 3085 differential mobility analyzer and TSI model 3776 condensation particle counter, 1/60 Hz) and a Laser Aerosol Spectrometer (LAS, TSI model 3340) were used to measure aerosol particles with diameter d between 3 and 100 nm and larger than 100 nm below the cloud base, respectively. Their uncertainty is within $\pm 10 - 20\%$ over the submicron aerosol size range (Moore et al., 2021). The measured aerosol size distributions are fitted with lognormal modes as shown in Figure S6a in Supporting Information S1 for the 02 June 2021 case and in Figure S6b in Supporting Information S1 for the 07 June 2021 case. The

corresponding fitted parameters are listed in Table S2 in Supporting Information S1. The flight-leg averaged total aerosol number concentration \bar{N}_a is 707 cm^{-3} and $2,073 \text{ cm}^{-3}$ for the 02 June and 07 June cases, respectively. Both cases feature the Aitken, accumulation, and coarse modes. The accumulation mode with the total aerosol number concentration $N_2 = 204 \text{ cm}^{-3}$ ($N_2 = 2,073 \text{ cm}^{-3}$), geometric median radius $\mu_2 = 98.5 \text{ nm}$ ($\mu_2 = 117.1 \text{ nm}$), standard deviation $\sigma_2 = 1.38$ ($\sigma_2 = 1.25$), and hygroscopicity $\bar{\kappa} = 0.55$ ($\bar{\kappa} = 0.35$) for the 02 June (input of simulation 0602_NA1) (07 June; input of simulation 0607_NA1) case, dominates the activation. More detailed information is listed in Table S2 in Supporting Information S1. The vertical structure of N_a is derived using combined polarimetric and lidar remote sensing observations (Schlosser et al., 2022). The retrieved vertical structure of N_a exhibits exponential decay with height (Figure S7 in Supporting Information S1). Our LES takes the lognormal distributions as aerosol input, which follows this exponential decay with height in the simulation domain.

2.1.3. Estimated Hygroscopicity

The bulk hygroscopicity ($\bar{\kappa}$) of aerosol particles for each lognormal size mode is estimated from κ and mass fraction of each chemical component m_i following the volume mixing rule (Petters & Kreidenweis, 2007). The m_i (listed in Table S3 in Supporting Information S1) is measured by an Aerodyne High Resolution Time-of-Flight Aerosol Mass Spectrometer (HR-ToF-AMS) (DeCarlo et al., 2008) with an uncertainty up to 50%. The estimated bulk hygroscopicity $\bar{\kappa}$ for aerosol particles larger than 60 nm in diameter d is listed in Table 1 and Table S4 in Supporting Information S1, which is used for the second and third mode of the lognormal distribution. For aerosol particles with $d \leq 60 \text{ nm}$ (first mode of the lognormal distribution) that lack valid measurements, we use the smallest value of the organic component $\kappa = 0.014$ and the mean value $\kappa = 0.1$ for the 02 and 07 June cases, respectively. We adopt such treatment of estimating $\bar{\kappa}$ for two reasons. First, measuring mass fraction of aerosol particles with $d \leq 60 \text{ nm}$ is very challenging with high uncertainties. Therefore, we use the estimated κ of the organic components from existing literature. Second, the smallest and mean κ value of the organic component as input yields the best matching cloud microphysical properties to the in-situ measurements for the 02 June and 07 June cases, respectively.

2.1.4. Measured Cloud Microphysical Properties

The cloud droplet size distribution, N_c , r_{eff} , and LWC were measured by FCDP. The FCDP can measure cloud droplets with diameter ranging from 3 to 50 μm with an uncertainty of less than 20% (Baumgardner et al., 2017; Knop et al., 2021). Cloud particles larger than 50 μm are measured by the 2DS probe (Lawson et al., 2006) with a spatial resolution of 11.4 $\mu\text{m}/\text{pixel}$ (Bansmer et al., 2018; Voigt et al., 2010). The 2DS covers a size range of 28.5–1,464.9 μm in this study.

2.1.5. Reanalysis and Satellite Data

Since the idealized LES cannot capture the large-scale motions of the atmospheric flow, we use the fifth generation of European Centre for Medium-Range Weather Forecasts's Integrated Forecast System (ERA5)

reanalysis (hourly model-level and single-level with a mesh grid-size of 31 km) large-scale forcings (i.e., moisture and temperature advective tendencies and wind profiles) and surface heat fluxes to drive the LES (X.-Y. Li et al., 2022, 2023). LWP retrieved from hourly single-level (quantities obtained from the model level) ERA5 and the Modern-Era Retrospective analysis for Research and Applications version 2 (MERRA-2) (starting from 00:30 UTC) is used for comparison with WRF-LES results and observations. The mean ERA5 (MERRA-2) LWP is calculated by averaging model grids over the dropsonde-covered area. Both ERA5 (hourly) and MERRA-2 (3-hourly) provide the CFC field at individual model levels, from which the time evolution of CFC is obtained by averaging the maximum values of the CFC vertical-profiles obtained by sampling each layer conditionally with a threshold of $LWC = 0.01 \text{ g cm}^{-3}$ for clouds below 7 km. Both LES and ERA5 and MERRA-2 reanalysis results are compared to the GOES-16 product, the first of the GOES-R series of the Geostationary Operational Environmental Satellites (GOES). The GOES-16 cloud retrievals we use in this study have a pixel size of 2 km and a time interval of 20 min.

ERA5, MERRA-2, and GOES-16 data are averaged over the dropsonde area. The GOES-16 LWP, N_c , and r_{eff} data are filtered by a cloud optical depth threshold ≥ 3 to limit the systematic biases in LWP and r_{eff} following the procedure described in Painemal and Zuidema (2011) and Painemal et al. (2021).

2.1.6. Instruments

The list of instruments and their measurements used in this study is shown in Table S1 in Supporting Information S1. We refer to Sorooshian et al. (2023) for a complete list of instruments deployed during the ACTIVATE campaign.

2.2. LES Numerical Experiment Design

To study the impact of observed aerosols on clouds for the two selected cases, we perform LES with measured aerosol size distribution from two different below cloud base (BCB) legs under the same meteorology conditions and large-scale forcings. This enables us to distinguish the aerosol impact on clouds from the meteorology impact. In addition, such configuration also allows us to utilize the in-situ measurements of cloud and aerosols to quantitatively study ACI. To test the ACI sensitivity to N_a , we also artificially change N_a with fixed μ and σ of aerosol size distribution from a BCB leg.

The Weather Research and Forecasting (WRF) model (Gustafson et al., 2020; Skamarock et al., 2019) in the idealized LES mode (WRF-LES), that is, periodic boundary condition in horizontal directions (Wang et al., 2009), is used in this study. The LES domain has a lateral size of $L_x = L_y = 20 \text{ km}$ with a grid spacing of $dx = dy = 100 \text{ m}$ and a vertical extent of $z_{\text{top}} = 7 \text{ km}$ with 153 vertical layers. Although our sensitivity tests with $dx = dy = 300 \text{ m}$ produce deeper clouds (closer to the measurements) than the ones with $dx = dy = 100 \text{ m}$ (Figures S10 and S13 in Supporting Information S1), we use a 100 m horizontal grid spacing to resolve smaller turbulent eddies that are important for the formation and evolution of shallow cumuli. Time-varying, area-averaged temperature and moisture advective tendencies ($\partial_t \bar{\theta}$ & $\partial_t \bar{q}_v$), divergence (\bar{D}), and surface turbulent heat fluxes are obtained from ERA5 for both cases except that the largest hourly surface heat fluxes among all the ERA5 grids within the dropsonde circle area are used for the 07 June 2021 case. A relaxation time scale of 3 hr is applied to nudge θ and q_v above 3 km and 1 hr for u and v in the entire domain to ERA5 for both cases. This nudging strategy produces the best match of simulated meteorological states to the dropsonde measurements and cloud properties (especially CTH) to the in-situ measurements. We adopt the Eulerian forcing instead of the Lagrangian one (forcing derived following the Lagrangian trajectory of the air mass) because the former leads to more comparable clouds to the observations (see the comparison between them in Figures S14–S16 in Supporting Information S1). The CAM radiative transfer model and a constant sea surface albedo of 0.06 are used. The Coriolis force corresponding to the center location of model domain is applied to all simulations.

The two-moment Morrison cloud microphysics scheme (Morrison et al., 2009) with prescribed aerosol size modes (see Section 2.1.2) and hygroscopicity (see Section 2.1.3) is employed, as initially implemented by Endo et al. (2015). Simulations with prescribed aerosol size distributions derived from the ACTIVATE campaign measurements, as described in Section 2.1.2, are performed for both cases. We use prescribed aerosol size distribution instead of the prognostic one as in Erfani et al. (2022) because a prognostic aerosol model requires accurate information about particle and gas emissions to reproduce the observed aerosol size distributions. All simulations start at 06:00 UTC and end at 21:00 UTC with a fixed time step of 1 s. Initial profiles of temperature,

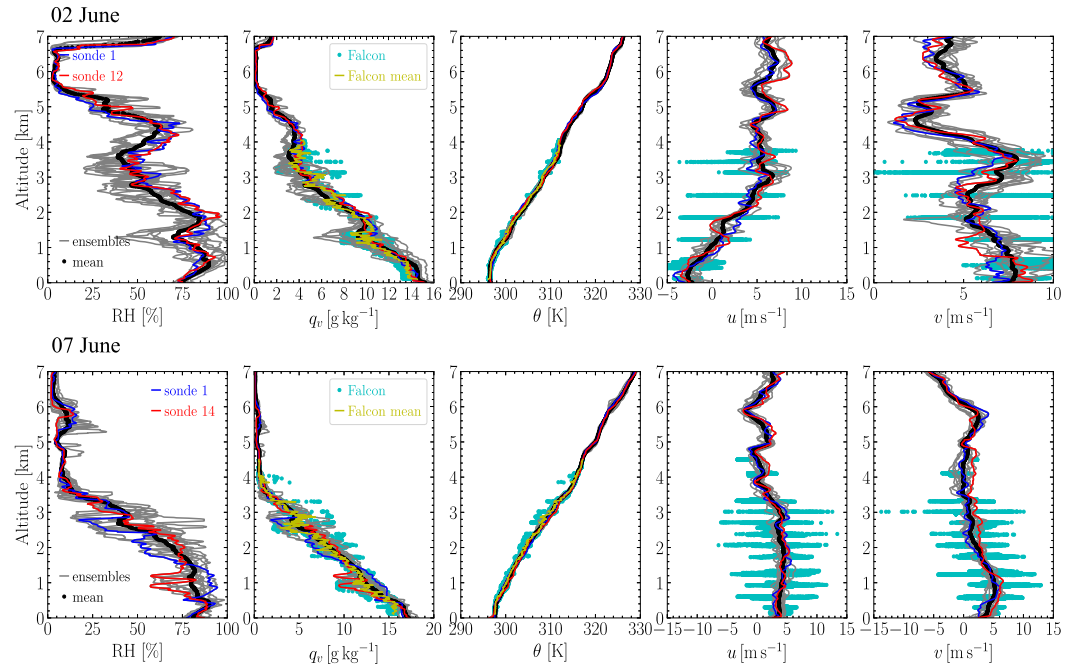


Figure 1. Profiles from dropsonde and Falcon measurements up to 7 km (same as the large-eddy simulations vertical domain size) for the 02 June (upper row) and 07 June (lower row) 2021 cases. The blue and red curves represent the first and last dropsonde, respectively, released at about the same location but 1 hour apart. The gray lines represent dropsonde in between, and the thick black lines represent the corresponding mean profile. The cyan dots show all the data points from the Falcon measurement (up to ~4 km) during the dropsonde measurement time. The yellow lines represent the averaged Falcon measurement every 10 m vertically to approximately match the vertical spacing of dropsonde profiles.

humidity, and winds for all simulations are obtained from the corresponding ERA5 profiles averaged over the targeted case domain at 06:00 UTC. We refer to Table 1 for the input N_a , N_c , and $\bar{\kappa}$ of simulations.

3. Results

3.1. Aerosol Effect on Precipitating Cumuli: 02 June 2021 Case

The 02 June 2021 case is characterized by heavier precipitation. The meteorology state from the dropsonde measurements exhibits strong spatial variation of RH (q_v) by comparing the gray curves (individual dropsonde) and black curve (mean profile) as shown in Figure 1a. The strong spatial variation of q_v makes the simulation of this case challenging. The mean q_v -profile from the Falcon measurement (yellow curve) agrees with the dropsonde measurement. The instantaneous Falcon measurements (cyan dots) within the dropsonde circle for each case show strong spatiotemporal variations as well. The meteorology state from LES is evaluated against the dropsonde measurements. Compared to dropsonde measurements, all simulations yield colder θ and larger q_v below about 3.5 km and vice versa above, as shown in Figures 2a and 2b. We then compare the cloud properties between LES and the FCDP measurements. The three simulations (red, cyan, and orange squares) capture the measured LWC (black squares) as shown in Figure 3a. In contrast, simulation 0602_NA1 and 0602_NA2 overestimates (underestimates) N_c (r_{eff}) as shown in Figures 3b and 3c by comparing the red and cyan squares to black ones. Simulation 0602_NA3, which is perturbed by halving N_a of simulation 0602_NA1 (orange squares), yields the closest N_c and r_{eff} to the FCDP measurements, even though 0602_NA1 is forced by the directly measured aerosol size distribution from a BCB leg. This highlights the complexity of comparing the LES outputs and in-situ measurements. Overall, our simulations capture the observed cloud properties reasonably well despite the aforementioned challenges.

To quantify the aerosol effect on precipitating cumuli, we adopt the metric of percentage difference (PD), defined as $\text{PD} = \frac{(Q_{\text{NA3}} - Q_{\text{NA1}})}{Q_{\text{NA1}}} \times 100\%$ with Q_{NA1} and Q_{NA3} representing quantities (X.-Y. Li et al., 2023) from the NA1 (baseline) and NA3 simulations, respectively. Q is averaged between 08:00 and 20:00 UTC (Table S5 in

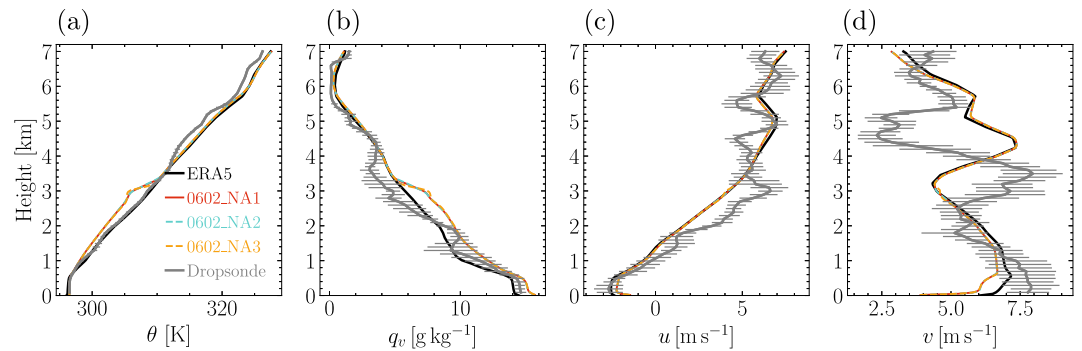


Figure 2. Domain-averaged vertical profiles from the WRF-LES simulations with the corresponding input forcings shown in Figure S24 in Supporting Information S1 at the measurement time for the 02 June 2021 case. The black line represents the ERA5 reanalysis data and the red (0602_NA1), cyan (0602_NA2), and orange (0602_NA3) ones represent the WRF-LES averaged values during the measurement time. The gray curves represent the dropsonde measurement with $\pm\sigma$ error bars.

Supporting Information S1). Here, we focus on comparing simulation 0602_NA1 and 0602_NA3 as only N_a is perturbed (halved) while κ , μ , σ and the vertical structure of aerosol size distribution are kept the same between the two simulations. Simulation 0602_NA3 yields 48.2% smaller (18.4% larger) N_c (r_{eff}) compared to 0602_NA1 as shown by red stars (0602_NA1) and orange squares (0602_NA3) in Figures 4e and 4f, suggesting a significant Twomey effect (Twomey, 1977). A decreased N_c due to the N_a reduction enhances the precipitation (i.e., the Rain Water Path (RWP) shown in Figure 4d is increased by 80.4%), which leads to a 5.8% decrease of LWP as shown by red stars and orange squares in Figure 4a. This LWP adjustment is consistent with the findings in Albrecht (1989), which suggested that increasing CCN decreases the drizzle production and therefore increases the LWP for shallow marine clouds. CFC from simulation 0602_NA3 (orange squares in Figure 4b) is smaller until 17:00 UTC and then becomes larger compared to 0602_NA1 (red stars in Figure 4b). Overall, halving N_a leads to a 17.7% increase of CFC in this case, which is contrary to a decrease in CFC as suggested in Albrecht (1989). CFC increases and then decreases monotonically with RWP. The timing of the CFC peak is

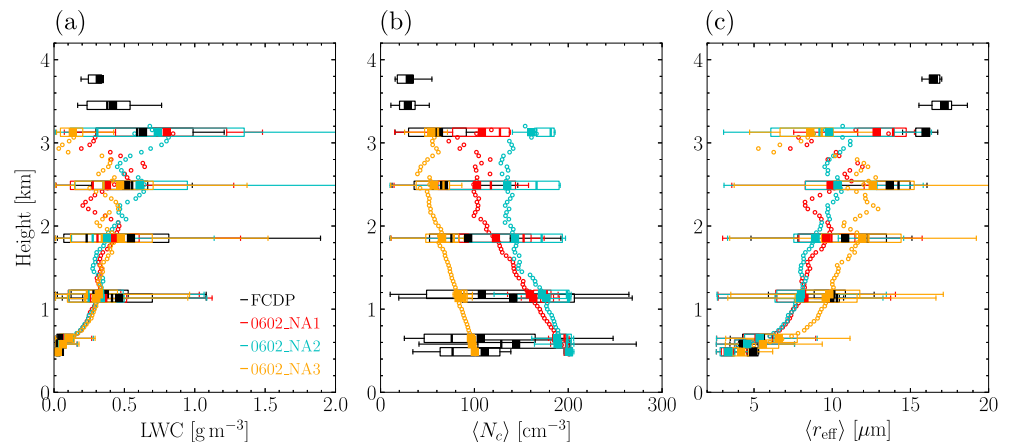


Figure 3. Comparison of vertical profiles of liquid water content (LWC), $\langle N_c \rangle$, and $\langle r_{eff} \rangle$ between the WRF-LES (0602_NA1, 0602_NA2, and 0602_NA3 listed in Table 1) and the fast cloud droplet probe (FCDP) measurements (black). A threshold of $LWC = 0.01 \text{ g m}^{-3}$, effective diameter $d_{eff} = 3.5 \text{ } \mu\text{m}$ and $N_c = 10 \text{ cm}^{-3}$ is applied to both the WRF-LES and the FCDP data. For the WRF-LES, only grid cells within clouds are averaged to obtain the vertical profile. The corresponding mean vertical profile of LWC, $\langle N_c \rangle$, and $\langle r_{eff} \rangle$ is obtained by averaging three snapshots of WRF-LES output (30 min apart). We only used above cloud base and below cloud top flight legs. The data are binned at those heights with a residual range of $\pm 50 \text{ m}$ such that at least one model layer is counted at the height of each flight legs. Smaller residual ranges do not affect the statistics. In the box-and-whisker plot, the binned data extends horizontally from the 25th (Q1, l.h.s wall of the box) to the 75th (Q2, r.h.s wall of the box) percentile with the median represented by the splitting line inside the box, the mean represented by solid squares inside the box, the minimum (Q_{min}) and maximum (Q_{max}) values represented by the left and right end of whiskers, respectively, and the outliers (values larger than $Q_{max} + 1.5(Q2 - Q1)$ and smaller than the $Q_{min} - 1.5(Q2 - Q1)$) represented by open circles. Here Q denotes values of a quantity (i.e., LWC, $\langle N_c \rangle$, and $\langle r_{eff} \rangle$).

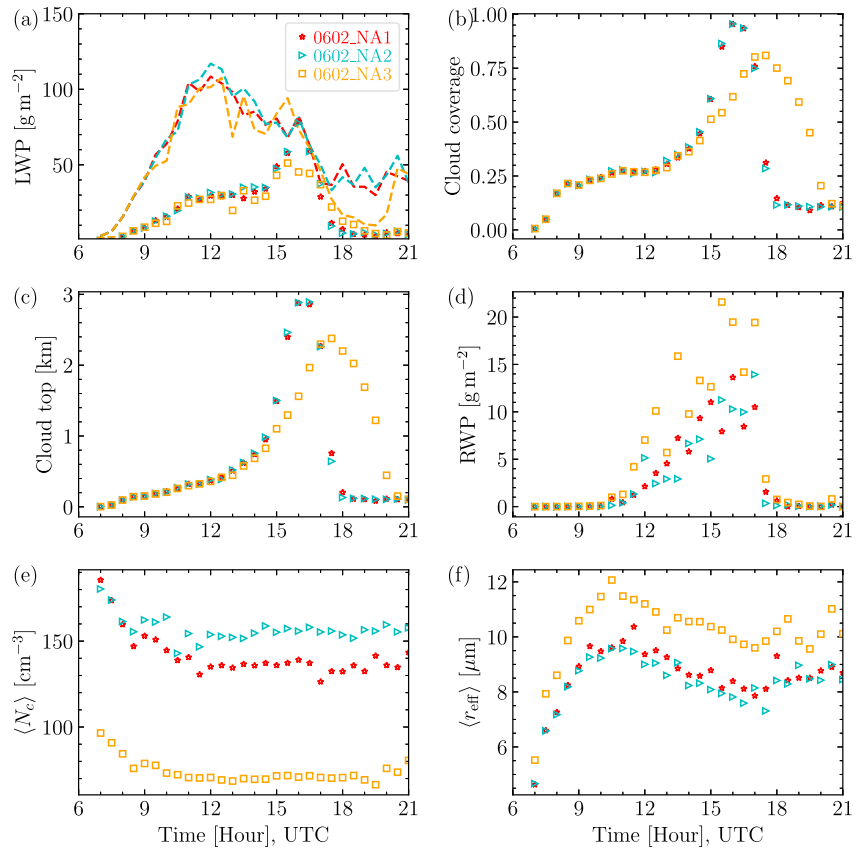


Figure 4. Time series of cloud properties for the 02 June 2021 case. Liquid water path is shown as domain-averaged (symbols) and cloud-averaged quantity (dashed lines) in panel (a). Cloud coverage is calculated as the ratio of the number of vertical columns, where $LWC \geq LWC^* = 0.01 \text{ g m}^{-3}$ in any model layers, to the total number of columns. Cloud top height is averaged over all cloudy columns. Rain water path is domain-averaged. N_c and r_{eff} are cloud-averaged.

consistent with the one of RWP evolution (Figure 4d). The SW cloud forcing at the top of the model increases by 6.0 W m^{-2} associated with the N_a reduction due to aerosol-cloud-precipitation interactions.

To quantify the aerosol effect on precipitation change, we examine the precipitation susceptibility defined as $S_o = -\Delta \ln \langle R_p \rangle / \Delta \ln \langle N_c \rangle$, where R_p is the precipitation rate derived from the accumulated total grid-scale surface precipitation of WRF-LES. The rain frequency (E_p) susceptibility $-\Delta \ln \langle E_p \rangle / \Delta \ln \langle N_c \rangle$ is also examined. Here, a threshold of $R_p > 0.004 \text{ mm hr}^{-1}$ is applied to each grid to define rain events, following Table 5 of Jiang et al. (2010). S_o is calculated from the spatiotemporal averaged R_p and N_c between perturbed and baseline simulations. The precipitation susceptibility to aerosol perturbation depends on the LWP threshold (Sorooshian et al., 2009) and cloud thickness (Jung et al., 2016). R_p is least susceptible to N_c for weakly precipitating shallow MBL clouds because of low LWP ($\leq 500 \text{ g m}^{-2}$), is less susceptible to deeper convective BL clouds because of the large abundance ($\geq 1,000 \text{ g m}^{-2}$) of LWP, and is most susceptible to MBL clouds with intermediate LWP ($\sim 500 - 1,000 \text{ g m}^{-2}$). R_p from simulation 0602_NA3 (orange squares with error bars) is larger than that from 0602_NA1 (red stars), as shown in Figure 5a, because halving N_a leads to smaller N_c , larger droplet size, and stronger precipitation rate. Consistent with the aerosol effect on R_p , the precipitation event E_p is also enhanced in 0602_NA3, as shown by the dashed red and orange curves in Figure 5b when averaged between 08:00–20:00 UTC. This aerosol-induced suppression of precipitation is further quantified by a negative value of S_o (-0.13) between 0602_NA3 and 0602_NA1 simulations.

3.2. Aerosol Effect on Drizzling Cumuli: 07 June 2021 Case

Compared to the 02 June 2021 case, the 07 June 2021 one is initially more polluted, in which N_a is about three times larger, as shown in the second column of Table 1. As a result, only drizzle was observed for the 07 June case.

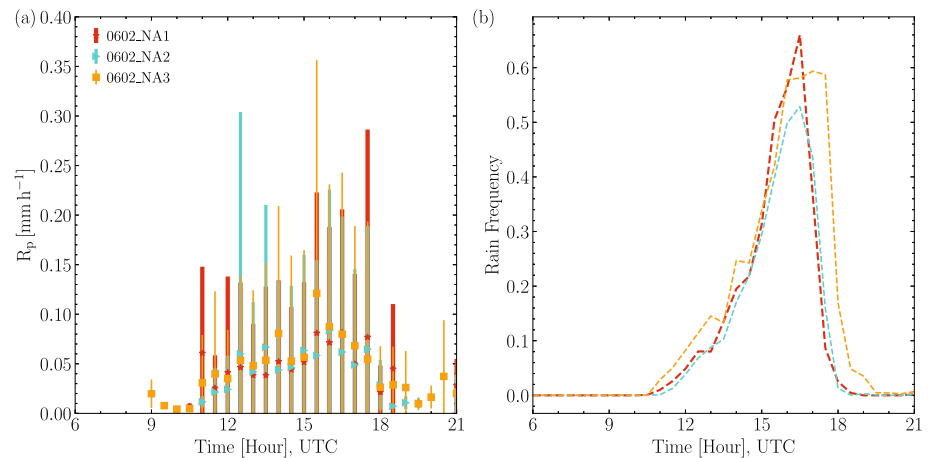


Figure 5. Precipitation rate (a) R_p (dots and pluses with error bars) and rain event frequency (b) E_p (dashed lines) for the 02 June 2021 case. See Table 2 for the S_o calculation.

We first compare the vertical profiles (meteorology states) amongst the dropsonde measurement, LES, and ERA5 data sets. All simulations can reproduce the θ -profile compared to the dropsonde measurement, except for a warmer free troposphere between 4 and 6 km as shown in Figure 6a. LES produces a more humid boundary layer until 2 km compared to the dropsonde measurements and ERA5, as shown in Figure 6b. The LES horizontal wind components agree with the dropsonde measurements (Figures 6e and 6f). Overall, the LES captures the observed MBL meteorology states.

LES cloud microphysical properties for this case are also evaluated against the FCDP measurements. Figure 7 shows that the measured LWC and N_c exhibit a large spatial variability, but simulations 0607_NA1 (red symbols) and 0607_NA2 (cyan symbols) can reproduce the LWC and r_{eff} from the FCDP measurements well as shown in Figures 7a and 7c. Figure 7b shows 0607_NA1 (red symbols) captures FCDP- N_c between 1.5 and 2 km while 0607_NA2 (cyan symbols) only captures it between about 1.5 and 2.5 km.

After the evaluation of modeled meteorology state and cloud properties against the measurements, we now investigate the aerosol effect on drizzling (i.e., weakly precipitating) cumuli by comparing simulation 0607_NA1 and 0607_NA3, where only N_a is perturbed. Compared to simulation 0607_NA1, N_a is doubled in 0607_NA3, which leads to an increased N_c (PD = 62.7%) and decreased r_{eff} (PD = 13.0%; the orange and red circles in Figures 7b and 7c). Aerosol effects on LWP (PD = 0.6%) and CFC (PD = 6.9%) are almost negligible by comparing the time evolution of domain-averaged LWP and CFC for simulation 0607_NA3 (orange squares) and 0607_NA1 (red stars) as shown in Figures 8a and 8b. This is likely because of the negligible precipitation as shown by the RWP in Figure 8d, which is similar to the wintertime ACTIVATE stratocumulus cases described in (X.-Y. Li et al., 2023). The light precipitation limits the precipitation-modulation pathway of ACI and, therefore, leads to a weak LWP and CFC response to N_a . Overall, the N_a perturbation mostly reflects the Twomey effect, although the aerosol induced RWP-reduction is 57.3%. The overall net cooling effect is negligible (0.002 W m^{-2})

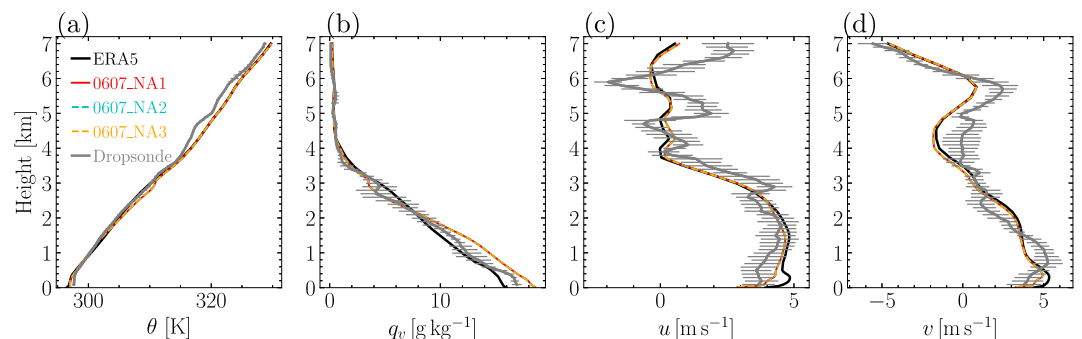


Figure 6. Same as Figure 2 but for the 07 June case.

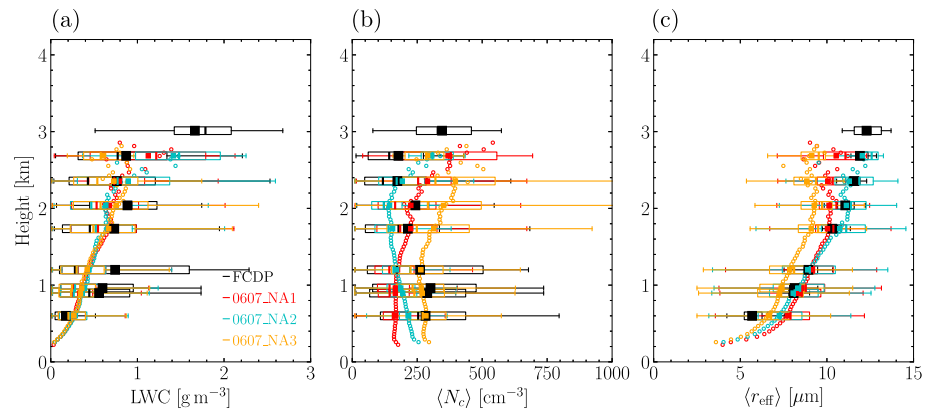


Figure 7. Same as Figure 3 but for the 07 June case.

in terms of SW cloud forcing at the top of the model. The simulated precipitation on 07 June is very weak with RWP on the order of 10^{-2} g m^{-2} as shown in Figure 8d, the precipitation susceptibility of which is therefore not discussed.

3.3. Aerosol-Induced LWP and CFC Adjustment: Entrainment and Precipitation

In this section, we examine the ACI induced by two different ways of perturbation. The first one is to perturb the N_a only as in the conventional fashion, that is, N_a of simulation 0602_NA3 is halved compared to 0602_NA1. The second one is to perturb the κ and aerosol size distribution based on measurements of aerosols BCB. Compared to the first perturbation method, this method is more realistic but rarely explored.

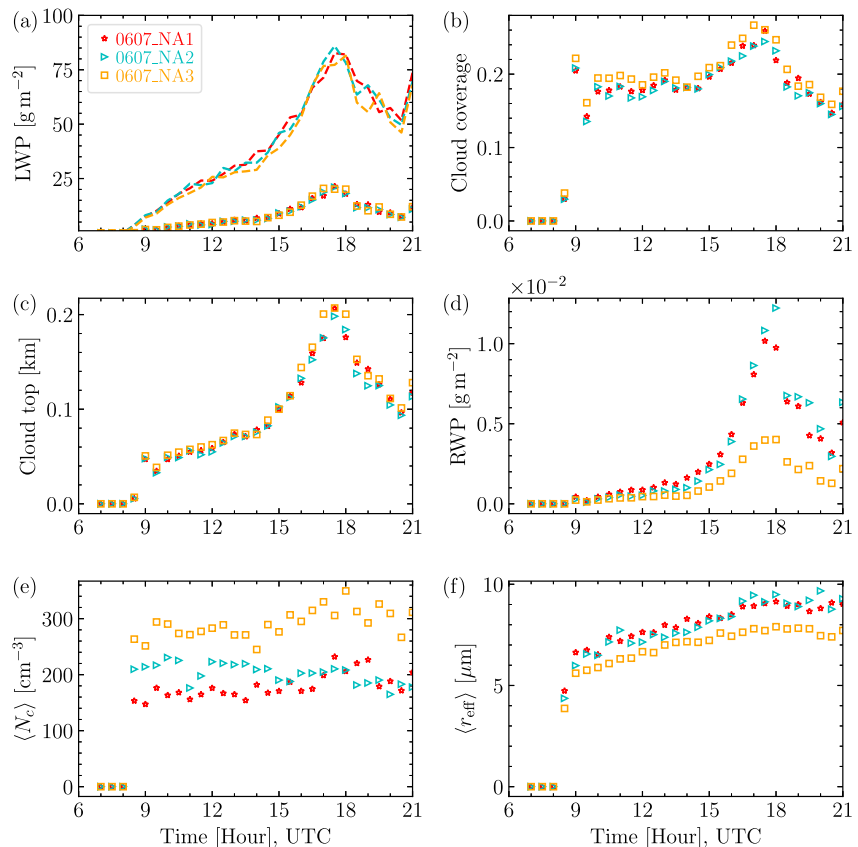


Figure 8. Same as Figure 4 but for the 07 June 2021 case.

Table 2

Aerosol Perturbation Induced Susceptibility of Liquid Water Path and r_{eff} to N_c (Cloudy Average) Between 08:00 and 20:00 UTC for the 02 and 07 June 2021 Cases

Case	$\Delta \ln \overline{\text{LWP}} / \Delta \ln \langle N_c \rangle$	$-\Delta \ln \langle r_{\text{eff}} \rangle / \Delta \ln \langle N_c \rangle$	$\Delta \ln \overline{\tau_c} / \Delta \ln \langle N_c \rangle$	$-\Delta \ln \overline{R_p} / \Delta \ln \langle N_c \rangle$	$-\Delta \ln \overline{E_p} / \Delta \ln \langle N_c \rangle$
0602 NA3-NA1	0.14	0.26	0.40	-0.13	0.43
0607 NA3-NA1	-0.124	0.29	0.16	-	-

Note. The LWP is cloud-averaged.

We first study the N_a -induced ACI by comparing simulation 0602_NA3 and 0602_NA1 and 0607_NA3 and 0607_NA1 for the 02 and 07 June cases, respectively. As discussed in Section 1, the LWP adjustment to aerosol-induced N_c , $\Delta \ln \overline{\text{LWP}} / \Delta \ln \langle N_c \rangle$, is nonlinear and depends on cloud regimes. In this section, we examine $\Delta \ln \overline{\text{LWP}} / \Delta \ln \langle N_c \rangle$ for the two cases studied here and contributing factors, that is, precipitation and cloud top entrainment. $\Delta \ln \overline{\text{LWP}} / \Delta \ln \langle N_c \rangle$ is calculated by averaging the time series of LWP and $\langle N_c \rangle$ between 08:00 and 20:00 UTC. The positive value, $\Delta \ln \overline{\text{LWP}} / \Delta \ln \langle N_c \rangle = 0.14$ for the 02 June case (simulation 0602_NA3 and 0602_NA1, Table 2), indicates a precipitation-dominated LWP adjustment, which leads to thicker and more reflective clouds. This is consistent with previous LES (Glassmeier et al., 2021) and satellite (Christensen et al., 2022) studies. For the polluted and lightly drizzling 07 June case, the negative $\Delta \ln \overline{\text{LWP}} / \Delta \ln \langle N_c \rangle = -0.124$ (simulation 0607_NA3 and 0607_NA1) appears to indicate an entrainment-dominated LWP adjustment. The aerosol impact on the cloud radiative effect can be quantified by the perturbation of cloud optical depth τ_c to N_c as (Ghan et al., 2016),

$$\frac{\Delta \ln \overline{\tau_c}}{\Delta \ln \langle N_c \rangle} = \frac{\Delta \ln \overline{\text{LWP}}}{\Delta \ln \langle N_c \rangle} - \frac{\Delta \ln \langle r_{\text{eff}} \rangle}{\Delta \ln \langle N_c \rangle}. \quad (1)$$

Equation 1 shows that both the Twomey effect (second term) and the cloud macrophysical adjustment (first term) contribute to τ_c . For the 02 June case, the Twomey effect (0.26) and LWP adjustment (0.14) terms are comparable, which leads to a positive $\Delta \ln \overline{\tau_c} / \Delta \ln \langle N_c \rangle$ of 0.40. For the 07 June case, the Twomey effect (0.29) and a negative LWP adjustment effect (-1.24) leads to $\Delta \ln \overline{\tau_c} / \Delta \ln \langle N_c \rangle = 0.16$.

We further examine the ACI metrics from simulations using aerosol size distributions and κ obtained from different BCB flight legs (“NA2” vs. “NA1”) for both cases. Simulation 0602_NA2 is the same as 0602_NA1 but with aerosols measured from another BCB flight leg. The vertical structure of LWC, N_c , and r_{eff} from these two simulations are very different during the measurement time as shown in Figure 3 because the vertical structure of the input aerosol size distributions are different (gray curves in Figures S7a and S7b in Supporting Information S1), which leads to a strong vertical variation of $\Delta \ln \text{LWC} / \Delta \ln N_c$, $\Delta \ln r_{\text{eff}} / \Delta \ln N_c$, and $\Delta \ln \tau_c / \Delta \ln N_c$ as shown by cyan curves in Figures 9a–9c, respectively. The time evolution of the vertical profiles also exhibit strong spatiotemporal variations as shown in Figure S17a–S17c in Supporting Information S1, respectively, from which we see that the $\Delta \ln \text{LWC} / \Delta \ln N_c$ dominates $\Delta \ln \tau_c / \Delta \ln N_c$ over $\Delta \ln r_{\text{eff}} / \Delta \ln N_c$. The mean ACI metrics are not used here because they average out the vertical variability of ACI. The vertical structures of N_a -induced ACI (simulation 0602_NA3-0602_NA1, orange curves in Figure 9) exhibit less vertical variation compared to the aerosol size distribution-induced (cyan curves in Figure 9) one, as expected. The same conclusions can be drawn for the 07 June case, of which the ACI vertical structure during the measurement time and their time evolution are shown in Figures 9e–9g and Figure S18 in Supporting Information S1. We note that the effect of $\bar{\kappa}$ on ACI should be negligible in this study as $\bar{\kappa} = 0.55$ and $\bar{\kappa} = 0.53$ for simulation 0602_NA1 and 0602_NA2, respectively. For the 07 June case, $\bar{\kappa} = 0.35$ and $\bar{\kappa} = 0.30$ for simulation 0607_NA1 and 0607_NA2 as listed in the last column of Table 1, respectively. Therefore, we attribute the ACI variation to aerosol size distributions measured from different BCB legs for both cases.

Entrainment is another important process contributing to cloud macrophysical adjustments. We first examine the 02 June 2021 case. As shown in Figure 10a, w_e are almost identical for the three simulations while LWP exhibit noticeable differences even though w_e and LWP are anti-correlated with a Pearson correlation efficient of -0.64 (p -value = 0.004), -0.64 (p -value = 0.004), -0.56 (p -value = 0.017) for 0602_NA1 (red), 0602_NA2 (cyan), 0602_NA3 (orange) between 12:00–20:30 UTC (17 snapshots are used for the statistics). The correlation between the SW radiative flux at the model top (Figure S27a in Supporting Information S1) and w_e is rather poor with a

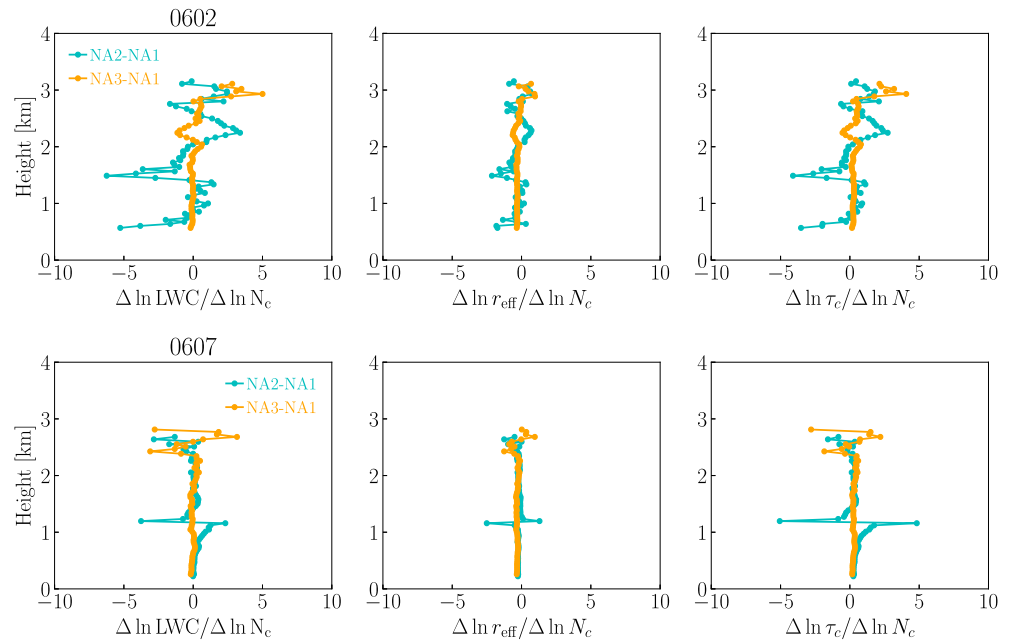


Figure 9. Aerosol-cloud interaction of vertical profiles shown in Figures 3 and 7. The evolution of vertical profiles is shown in Figures S17 and S18 in Supporting Information S1.

Pearson correlation coefficient of 0.37 (p -value = 0.13), 0.38 (p -value = 0.119), and 0.09 (p -value = 0.721) for simulation 0602_NA1 (red), 0602_NA2 (cyan), 0602_NA3 (orange), respectively.

For the 07 June case, both w_e (Figure 10b) and the domain mean LWP (Figure 13a) between simulation 0607_NA1 (red), 0607_NA2 (cyan), 0607_NA3 (orange) are almost identical. This indicates that the cloud top entrainment process has negligible feedback to the aerosol-induced LWP adjustment for the weakly drizzling cumuli even though w_e is anti-correlated with LWP (Figure 10b) with a Pearson correlation coefficient of -0.51 (p -value = 0.031), -0.58 (p -value = 0.012), and -0.6 (p -value = 0.009) for simulation 0607_NA1 (red), 0607_NA2 (cyan), 0607_NA3 (orange), respectively. The net SW radiative flux at the model top (Figure S27b in Supporting Information S1) shows positive correlation with the w_e with a Pearson correlation coefficient of 0.61 (p -value = 0.007), 0.63 (p -value = 0.005), and 0.66 (p -value = 0.003) for simulation 0607_NA1 (red), 0607_NA2 (cyan), 0607_NA3 (orange), respectively. Since the time-varying large-scale vertical velocity profile

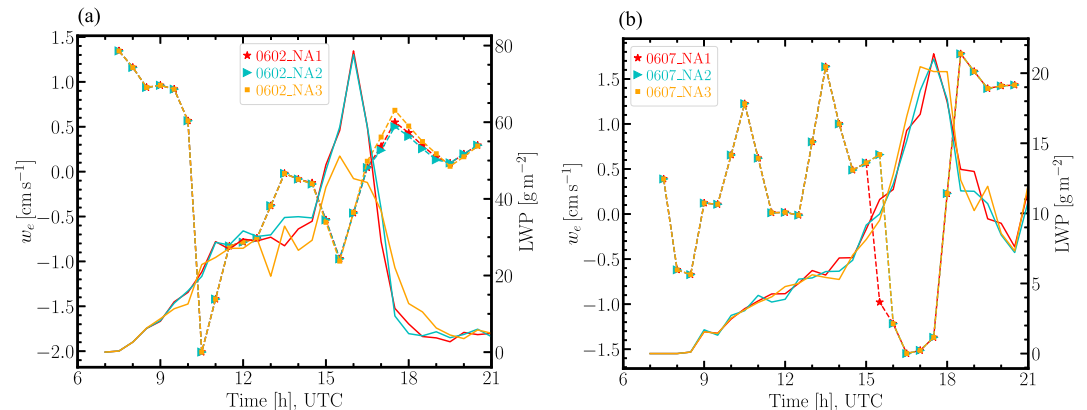


Figure 10. Entrainment rate $w_e = dz_i/dt - \langle w \rangle_{z_i}$ (symbols with dashed lines) and liquid water path (solid lines) for the 02 (a) and 07 (b) June 2021 cases, where the cloud top height z_i is determined by the threshold $LWC \geq 0.01 \text{ g m}^{-3}$. $\langle w \rangle_{z_i}$ is the ERA5 large-scale vertical velocity at z_i . The cloud top shortwave radiation is shown in Figure S27 in Supporting Information S1.

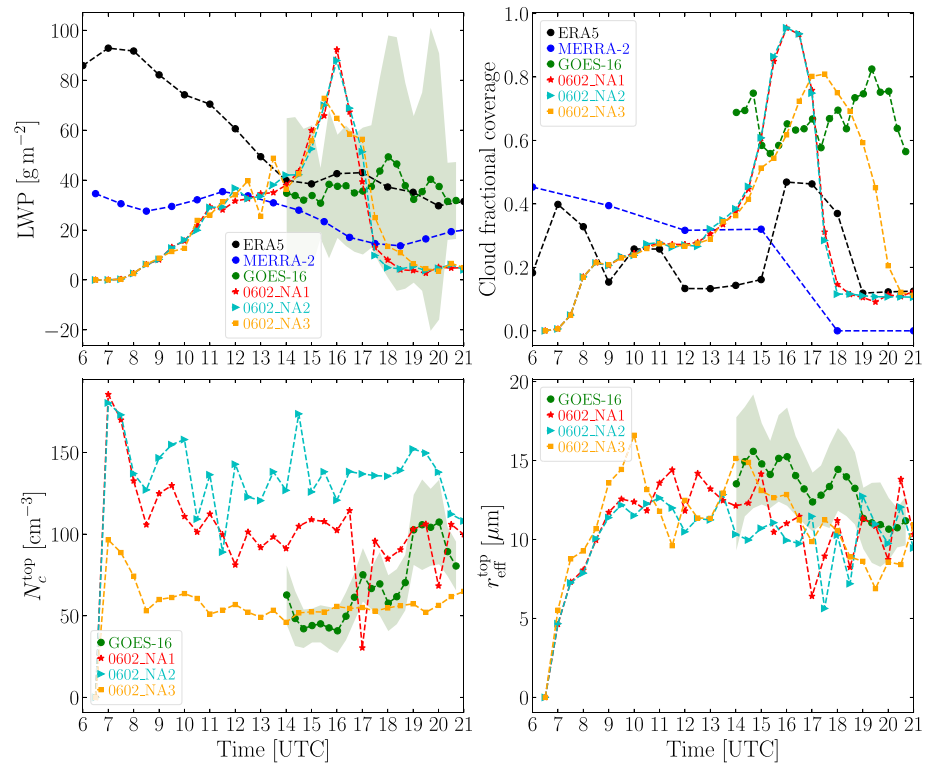


Figure 11. Comparison of cloud properties between the WRF-LES (0602_NA1, 0602_NA2, and 0602_NA3 in red, cyan, and orange, respectively), ERA5 (black), MERRA-2 (blue), and GOES-16 (green) for the 02 June 2021 case. The domain-averaged liquid water path includes both cloud and rain water. N_c^{top} and $r_{\text{eff}}^{\text{top}}$ are averaged (cloudy grid with $\text{LWC} \geq 0.01 \text{ g m}^{-3}$) over the cloud top (200 – 300 m) from the WRF-LES output. The shaded area represents $\pm\sigma$ of the spatial variation of GOES-16- N_c^{top} and $r_{\text{eff}}^{\text{top}}$. A comparison of the vertical profiles is shown in Figure 12.

(based on ERA5 forcing) $\langle w \rangle_{z_i}$ is the same for the three simulations, Δw_e is due to the dz_i/dt , which is caused by the difference in cloud properties and consequent radiative impact on boundary layer structure.

3.4. Evaluation of Large-Scale Models Using LES

To evaluate the representation of cloud micro/macro-physics in large-scale models using LES and observations, we compare ERA5 and MERRA-2 to LES and GOES-16. We first evaluate the cloud properties from ERA5 and MERRA-2 against GOES-16. ERA5 (black dots) agrees well with the GOES-16 measurements (green dots) in LWP while MERRA-2 (blue dots) shows smaller LWP in 14:00–21:00 UTC, as shown in Figure 11a for the 02 June 2021 case. CFC from ERA5 and MERRA-2 is smaller compared to GOES-16 (Figure 11b). The inconsistency between the reanalysis products (ERA5 and MERRA-2) and GOES-16 retrievals suggests a lack of observational benchmark of the cloud properties studied here. One obvious reason for this discrepancy is the spatial resolution difference between reanalysis data and GOES-16. To this end, we compare GOES-16 and ERA5 against LES, which has the highest resolution to capture fine scales. The LES does not capture the spatial structure of LWP (Figure S19 in Supporting Information S1) or CFC (Figure 11b) compared to GOES-16. The LES N_c (r_{eff}) is larger (smaller) than GOES-16 as shown in Figures 11c and 11d. However, we note that the GOES-16 N_c is smaller than FCDP- N_c during the FCDP measurement time (18:30–19:12 UTC). The time evolution of the domain averaged CFC from ERA5 (black dots) exhibits the same diurnal cycle as the LES (red stars and cyan triangles) (Figure 11b). This motivates us to further compare the vertical profiles of CFC and LWC among LES, ERA5, and MERRA-2. Compared to LES, ERA5 exhibit higher clouds while MERRA-2 produces too low and little clouds as shown by the time evolution of CFC and LWC vertical profiles from the reanalysis data and LES in Figure 12. ERA5 captures deep convection in the morning with cloud top up to 6 km and transitions to cumulus in the afternoon (Figures 12a and 12d), while LES shows a locally initiated convection

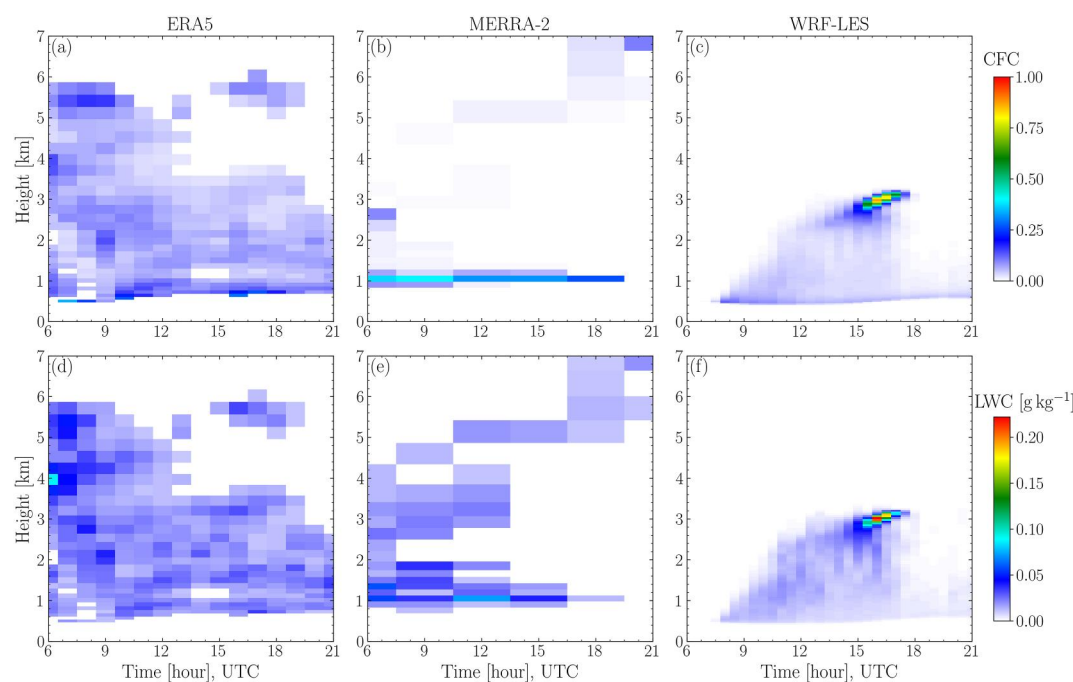


Figure 12. Evolution of vertical profile of cloud fractional coverage and liquid water content (LWC) for the 02 June 2021 case. They are obtained by sampling each layer conditionally with a threshold of $LWC = 0.01 \text{ g m}^{-3}$. The 0602_NA1 vertical profiles are calculated by normalizing the cloudy grids with the total number of grids (200×200) at each model level. ERA5 and MERRA-2 data are averaged over the dropsonde circle area.

(Figures 12c and 12f). Since LES is forced by the large-scale forcings derived from ERA5, the difference between LES and ERA5 (MERRA-2) may be attributed to fine scales captured only by LES.

For the 07 June 2021 case, the LES (red stars and cyan triangles) produces $\sim 1/3$ LWP of GOES-16 (green symbols) during 14:00–21:00 UTC, as shown in Figure 13a. The LES does not reproduce the GOES-16 LWP as shown in Figure S20 in Supporting Information S1. The CFC from LES is larger than that from GOES-16 (Figure 13b). The ERA5 LWP (black symbols) follows the same diurnal cycle as LES (red stars and cyan triangles) even though the magnitude is 2 times larger in 12:00–21:00 UTC (Figure 13b). This is remarkable considering the fact that cumuli hardly reach any steady state compared to the stratocumuli and that the ERA5 grid-spacing (30 km) is 300 times coarser than the LES (100 m). MERRA-2 (blue dots) has higher LWP than LES and ERA5. Neither the vertical structure of the ERA5 nor the MERRA-2 LWC resembles the ones from LES (Figures 14d and 14e). The cloud vertical extent from ERA5 (Figure 14d) reaches 3 km between 09:00–12:00 UTC and 6 km around 18:00 UTC compared to 2 km from the LES (Figure 14e). The ERA5 CFC agrees reasonably with the LES while the MERRA-2 CFC is smaller than LES as shown in Figure 13b. However, neither the ERA5 nor MERRA-2 capture the vertical structure of CFC compared to the LES (Figures 14a–14c). We note that LES underestimates the observed CTH by about 1 km compared to in-situ measurements. This again demonstrates the challenge in simulating precipitating cumulus even using LES. We remark that finding a benchmark for characterizing cumuli is very challenging due to limited observations (~ 1 -hr flight measurements), the coarse resolution of ERA5 (31 km), and small domain size of LES.

4. Discussions, Conclusions, and Outlook

We study aerosol-cloud-precipitation interactions in summertime precipitating shallow cumuli observed over the WNAO during the ACTIVATE campaign using LES. Two contrasting observational cases are selected. The 02 June 2021 case is a cleaner case featuring heavier precipitation, while the 07 June 2021 case is a more polluted one with lightly drizzling conditions. Both cases are very challenging to simulate due to the strong spatial variation of humidity and relatively deep boundary layer. For each case, the baseline LES is initiated with prescribed aerosol

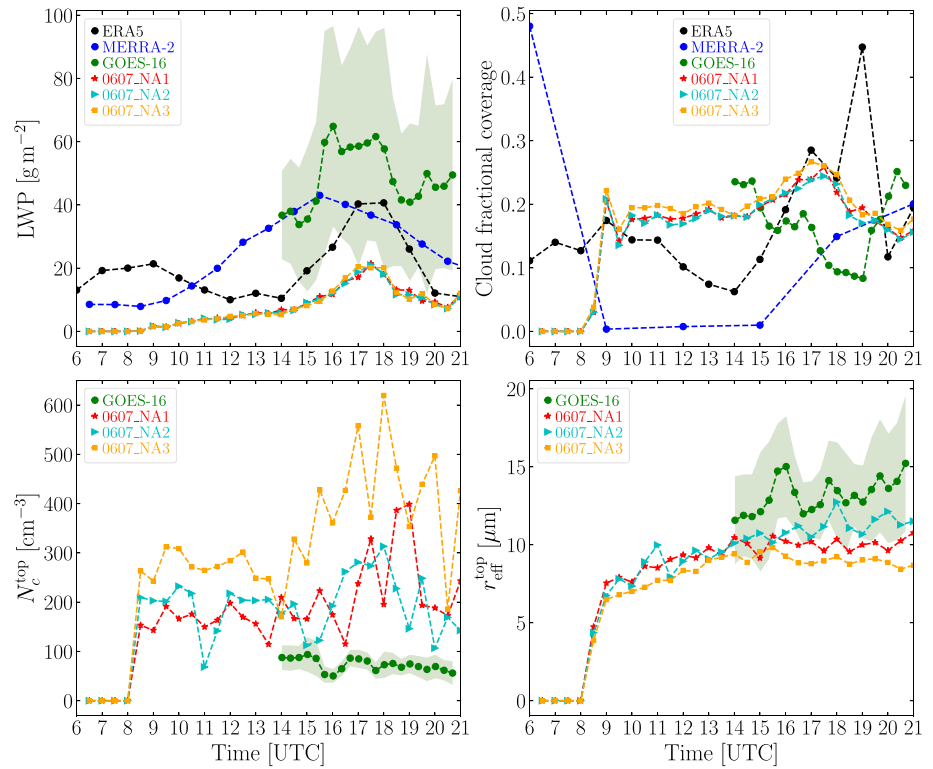


Figure 13. Same as Figure 11 but for the 07 June 2021 case. A comparison of the vertical profiles is shown in Figure 14.

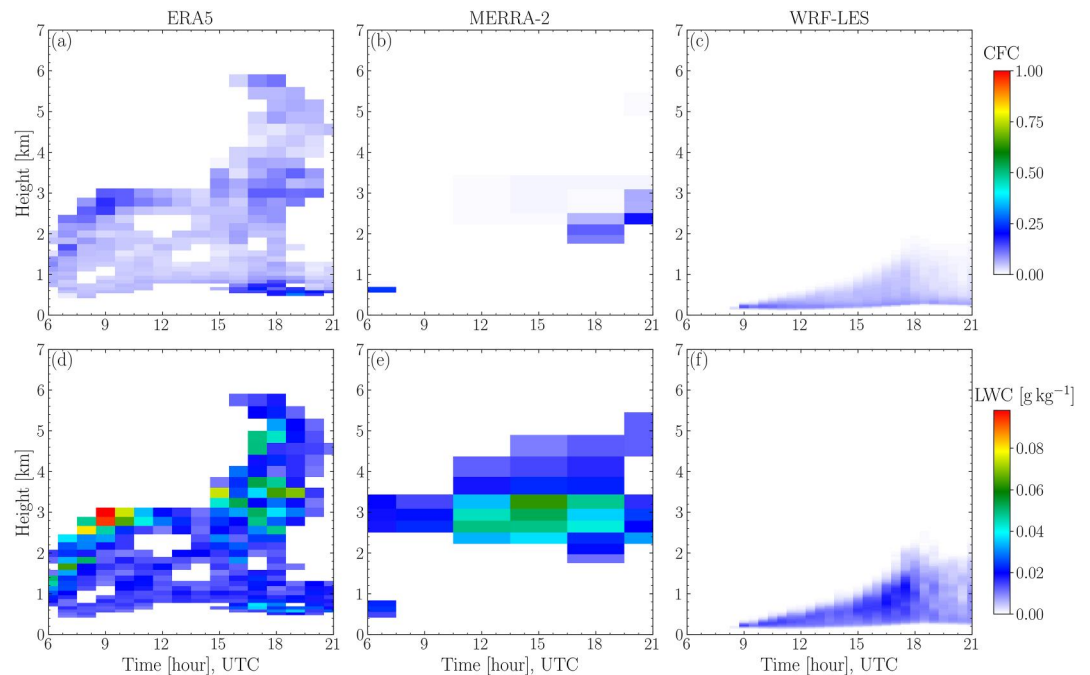


Figure 14. Same as Figure 12 but for the 07 June 2021 case.

size distributions derived from SMPS/LAS measurements and the hygroscopicity κ derived from the AMS measurements obtained from a BCB flight leg. To perturb the LES clouds, we performed sensitivity experiments either with changing N_a of the baseline simulation only (N_a -induced ACI) or with aerosol measurements from another flight leg during the same flight (aerosol size distribution-induced ACI). The LES experiments are forced by large-scale forcings, that is, advective tendencies of θ and q_v and surface heat fluxes from ERA5 reanalysis data. The simultaneous measurements of the meteorology state and cloud properties enable us to evaluate our LES results at both small and large scales that are essential for understanding ACI. For the 02 June 2021 case, LES yields a slightly colder and more humid MBL compared to the dropsonde measurements. LES can reproduce the FCDP measurements of cloud microphysical properties, which agree reasonably well with the satellite retrievals. For the 07 June 2021 case, LES captures the θ profile well but produces a more humid MBL. The cloud microphysical properties (LWC, N_c , and r_{eff}) from LES agree with FCDP measurements. Overall, the LES is able to reproduce the measured cloud microphysics although the spatial variability is challenging to simulate. To capture the spatial variability, we perform simulations using ERA5 large-scale forcings at the location of individual dropsonde (see Figures S21–S23 in Supporting Information S1), none of which reproduce the observed clouds. This shows the challenge in simulating fast-evolving marine cumuli. The LES fails to reproduce the spatial structure of LWP compared to GOES-16 and does not agree well with the satellite microphysics retrievals, even though the LES reproduces the LWP compared to the Research Scanning Polarimeter retrievals (Figure S26 in Supporting Information S1). The former could be because of the spatially uniform boundary conditions adopted in our LES that lack the mesoscale organizational structures shown in GOES-16 cloud field. The latter is likely due to both the idealized boundary conditions of the LES and uncertainties from the GOES-16 retrievals. The time evolution of LWP and CFC from ERA5 shows the same diurnal variation as LES for both cases although the fast-evolving subgrid shallow cumuli are challenging to simulate in ERA5 with much coarser spatiotemporal resolution than in LES.

For the clean precipitating 02 June case, The N_a -induced $\Delta \ln \overline{\text{LWP}} / \Delta \ln \overline{N_c} = 0.14$ (simulation 0602_NA3 and 0602_NA1, Table 2), suggesting precipitation-dominated LWP adjustments, which is consistent with many previous sensitivity studies of ACI. The CFC increases as N_c decreases despite a decreased LWP. To the best of our knowledge, it is the first time that this mechanism is tested in LES driven by measured cloud microphysics in the WNAO region. For the more polluted, lightly drizzling 07 June case, the negative LWP adjustment ($\Delta \ln \overline{\text{LWP}} / \Delta \ln \overline{N_c} = -0.124$) appears to suggest an entrainment-dominated ACI. However, the aerosol-induced changes in LWP and entrainment rate are very small for the weakly drizzling cumulus case, so the role of entrainment feedback remains unclear. The Twomey effect from the two cases are comparable (0.26 and 0.29 for the 02 and 07 June cases, respectively). For the aerosol size distribution-induced ACI, the ACI vertical structure of both cases exhibit strong spatiotemporal variations. The LWC adjustment $\Delta \ln \text{LWC} / \Delta \ln N_c$ dominates cloud optical depth adjustment $\Delta \ln \tau_c / \Delta \ln N_c$ over the Twomey effect $\Delta \ln r_{\text{eff}} / \Delta \ln N_c$. This suggests that quantifying ACI is more complex than the conventional mean ACI matrices as observed aerosol perturbations involve not only N_a , but also aerosol size distribution and κ .

The aerosol effect on precipitation rate is strongly nonlinear. The precipitation rate R_p has been argued to decrease with increasing aerosol number concentration N_a due to the suppression of collision-coalescence processes at fixed LWP in warm MBL (Albrecht, 1989). The assumption of a statistically steady LWP largely holds for stratocumuli (Glassmeier et al., 2021) but fails for the cumuli. This makes it challenging to quantify the precipitation susceptibility in cumuli. Negative precipitation susceptibility is observed for the precipitating 02 June 2021 case due to the decreased N_a that enhances the precipitation. R_p is less susceptible to N_c for the lightly drizzling 07 June 2021 case. Our finding is consistent with previous studies of the R_p – N_a relation for warm MBL clouds (Jung et al., 2016). Whether the aerosol effect on precipitation rate observed in the two cases here can be generalized to global scales remains to be investigated.

Summertime shallow cumuli over the WNAO region are characterized by fast-evolving and less strongly forced boundary layer, compared to wintertime stratocumuli, which makes it challenging to simulate even with LES. Initial meteorological conditions and large-scale forcings are critical for LES to capture the observed precipitating cumuli. However, with the same forcing conditions, there is a substantial difference in CFC and LWC vertical profiles between ERA5 (MERRA-2) and LES, which is not surprising and suggests that our understanding of the driving mechanisms of shallow convection and representation of cloud microphysics in models across scales

require improvement. Furthermore, the interplay between aerosols and clouds and its dependence on these driving mechanisms remains very uncertain.

Data Availability Statement

The source code used for the simulations of this study, the Weather Research and Forecasting model (Gustafson et al., 2020), is freely available on <https://code.arm.gov/lasso/lasso-wrf>. The simulations were performed using resources available through Research Computing at PNNL. Model input and output files (X. Li et al., 2023) are available at <https://doi.org/10.5281/zenodo.8034149>. ACTIVATE observational data (Team, 2020) are publicly available at <https://asdc.larc.nasa.gov/project/ACTIVATE>. GOES-16 data can be obtained at <https://satcorps.larc.nasa.gov/prod/exp/activate/visst-pixel-netcdf/g16-sd/2021/>. ERA5 reanalysis data (Hersbach et al., 2023) are available at <https://doi.org/10.24381/cds.adbb2d47>. MERRA-2 reanalysis data can be obtained at <https://disc.gsfc.nasa.gov/datasets?project=MERRA-2>.

Acknowledgments

This work was supported through the ACTIVATE Earth Venture Suborbital-3 (EVS-3) investigation, which is funded by NASA's Earth Science Division and managed through the Earth System Science Pathfinder Program Office. The Pacific Northwest National Laboratory (PNNL) is operated for the U.S. Department of Energy by Battelle Memorial Institute under contract DE-AC05-76RLO1830. S.K. and C.V. were funded by the Deutsche Forschungsgemeinschaft (DFG, German Research Foundation)—TRR 301—Project-ID 428312742. J.S.S. was supported by the NASA Postdoctoral Program at NASA Langley Research Center, administered by Oak Ridge Associated Universities under contract with NASA.

References

- Ackerman, A. S., Kirkpatrick, M. P., Stevens, D. E., & Toon, O. B. (2004). The impact of humidity above stratiform clouds on indirect aerosol climate forcing. *Nature*, *432*(7020), 1014–1017. <https://doi.org/10.1038/nature03174>
- Albrecht, B. A. (1989). Aerosols, cloud microphysics, and fractional cloudiness. *Science*, *245*(4923), 1227–1230. <https://doi.org/10.1126/science.245.4923.1227>
- Arola, A., Lipponen, A., Kolmonen, P., Virtanen, T. H., Bellouin, N., Grosvenor, D. P., et al. (2022). Aerosol effects on clouds are concealed by natural cloud heterogeneity and satellite retrieval errors. *Nature Communications*, *13*(1), 7357. <https://doi.org/10.1038/s41467-022-34948-5>
- Bansmer, S. E., Baumert, A., Sattler, S., Knop, I., Leroy, D., Schwarzenboeck, A., et al. (2018). Design, construction and commissioning of the Braunschweig Icing Wind Tunnel. *Atmospheric Measurement Techniques*, *11*(6), 3221–3249. <https://doi.org/10.5194/amt-11-3221-2018>
- Baumgardner, D., Abel, S. J., Axisa, D., Cotton, R., Crosier, J., Field, P., et al. (2017). Cloud ice properties: In situ measurement challenges. *Meteorological Monographs*, *58*(1), 1–9. <https://doi.org/10.1175/AMSMONOGRAPH5-D-16-0011.1>
- Bellouin, N., Quaas, J., Gryspeerdt, E., Kinne, S., Stier, P., Watson-Parris, D., et al. (2020). Bounding global aerosol radiative forcing of climate change. *Reviews of Geophysics*, *58*(1), e2019RG000660. <https://doi.org/10.1029/2019RG000660>
- Chen, Y.-C., Xue, L., Lebo, Z. J., Wang, H., Rasmussen, R. M., & Seinfeld, J. H. (2011). A comprehensive numerical study of aerosol-cloud-precipitation interactions in marine stratocumulus. *Atmospheric Chemistry and Physics*, *11*(18), 9749–9769. <https://doi.org/10.5194/acp-11-9749-2011>
- Christensen, M. W., Gettelman, A., Cermak, J., Dagan, G., Diamond, M., Douglas, A., et al. (2022). Opportunistic experiments to constrain aerosol effective radiative forcing. *Atmospheric Chemistry and Physics*, *22*(1), 641–674. <https://doi.org/10.5194/acp-22-641-2022>
- Christensen, M. W., Jones, W. K., & Stier, P. (2020). Aerosols enhance cloud lifetime and brightness along the stratus-to-cumulus transition. *Proceedings of the National Academy of Sciences of the United States of America*, *117*(30), 17591–17598. <https://doi.org/10.1073/pnas.1921231117>
- DeCarlo, P. F., Dunlea, E. J., Kimmel, J. R., Aiken, A. C., Sueper, D., Crouse, J., et al. (2008). Fast airborne aerosol size and chemistry measurements above Mexico City and Central Mexico during the MILAGRO campaign. *Atmospheric Chemistry and Physics*, *8*(14), 4027–4048. <https://doi.org/10.5194/acp-8-4027-2008>
- Diamond, M. S., Director, H. M., Eastman, R., Possner, A., & Wood, R. (2020). Substantial cloud brightening from shipping in subtropical low clouds. *AGU Advances*, *1*(1), e2019AV000111. <https://doi.org/10.1029/2019AV000111>
- Diskin, G. S., Podolske, J. R., Sachse, G. W., & Slate, T. A. (2002). Open-path airborne tunable diode laser hygrometer. In *Diode lasers and applications in atmospheric sensing* (Vol. 4817, pp. 196–204). International Society for Optics and Photonics. <https://doi.org/10.1117/12.453736>
- Endo, S., Fridlind, A. M., Lin, W., Vogelmann, A. M., Toto, T., Ackerman, A. S., et al. (2015). RACORO continental boundary layer cloud investigations: 2. Large-eddy simulations of cumulus clouds and evaluation with in situ and ground-based observations. *Journal of Geophysical Research: Atmospheres*, *120*(12), 5993–6014. <https://doi.org/10.1002/2014JD022525>
- Erfani, E., Blossey, P., Wood, R., Mohrmann, J., Doherty, S. J., Wyant, M., & O, K.-T. (2022). Simulating aerosol lifecycle impacts on the subtropical stratocumulus-to-cumulus transition using large-eddy simulations. *Journal of Geophysical Research: Atmospheres*, *127*(21), e2022JD037258. <https://doi.org/10.1029/2022JD037258>
- Gettelman, A., Hannay, C., Bacmeister, J. T., Neale, R. B., Pendergrass, A. G., Danabasoglu, G., et al. (2019). High climate sensitivity in the community Earth system model version 2 (CESM2). *Geophysical Research Letters*, *46*(14), 8329–8337. <https://doi.org/10.1029/2019GL083978>
- Ghan, S., Wang, M., Zhang, S., Ferrachat, S., Gettelman, A., Griesfeller, J., et al. (2016). Challenges in constraining anthropogenic aerosol effects on cloud radiative forcing using present-day spatiotemporal variability. *Proceedings of the National Academy of Sciences of the United States of America*, *113*(21), 5804–5811. <https://doi.org/10.1073/pnas.1514036113>
- Glassmeier, F., Hoffmann, F., Johnson, J. S., Yamaguchi, T., Carslaw, K. S., & Feingold, G. (2021). Aerosol-cloud-climate cooling overestimated by ship-track data. *Science*, *371*(6528), 485–489. <https://doi.org/10.1126/science.abd3980>
- Goren, T., Kazil, J., Hoffmann, F., Yamaguchi, T., & Feingold, G. (2019). Anthropogenic air pollution delays marine stratocumulus breakup to open cells. *Geophysical Research Letters*, *46*(23), 14135–14144. <https://doi.org/10.1029/2019GL085412>
- Gryspeerdt, E., Goren, T., Sourdeval, O., Quaas, J., Mülmenstädt, J., Dipu, S., et al. (2019). Constraining the aerosol influence on cloud liquid water path. *Atmospheric Chemistry and Physics*, *19*(8), 5331–5347. <https://doi.org/10.5194/acp-19-5331-2019>
- Gustafson, W. I., Vogelmann, A. M., Li, Z., Cheng, X., Dumas, K. K., Endo, S., et al. (2020). The large-eddy simulation (LES) atmospheric radiation measurement (ARM) symbiotic simulation and observation (LASSO) activity for continental shallow convection. *Bulletin of the American Meteorological Society*, *101*(4), E462–E479. <https://doi.org/10.1175/bams-d-19-0065.1>
- Hersbach, H., Bell, B., Berrisford, P., Biavati, G., Horányi, A., Muñoz Sabater, J., et al. (2023). ERA5 hourly data on single levels from 1940 to present. Copernicus Climate Change Service (C3S) Climate Data Store (CDS) [Dataset]. *Zenodo*. <https://doi.org/10.24381/cds.adbb2d47>

- Jiang, H., Feingold, G., & Sorooshian, A. (2010). Effect of aerosol on the susceptibility and efficiency of precipitation in warm trade cumulus clouds. *Journal of the Atmospheric Sciences*, *67*(11), 3525–3540. <https://doi.org/10.1175/2010JAS3484.1>
- Jung, E., Albrecht, B. A., Sorooshian, A., Zuidema, P., & Jonsson, H. H. (2016). Precipitation susceptibility in marine stratocumulus and shallow cumulus from airborne measurements. *Atmospheric Chemistry and Physics*, *16*(17), 11395–11413. <https://doi.org/10.5194/acp-16-11395-2016>
- Knop, I., Bansmer, S. E., Hahn, V., & Voigt, C. (2021). Comparison of different droplet measurement techniques in the Braunschweig Icing Wind Tunnel. *Atmospheric Measurement Techniques*, *14*(2), 1761–1781. <https://doi.org/10.5194/amt-14-1761-2021>
- Lawson, R. P., O'Connor, D., Zmarzly, P., Weaver, K., Baker, B., Mo, Q., & Jonsson, H. (2006). The 2D-S (stereo) probe: Design and preliminary tests of a new airborne, high-speed, high-resolution particle imaging probe. *Journal of Atmospheric and Oceanic Technology*, *23*(11), 1462–1477. <https://doi.org/10.1175/JTECH1927.1>
- Li, X., Wang, H., Christensen, M. W., Chen, J., Tang, S., Kirschler, S., et al. (2023). Dataset for paper “process modeling of aerosol-cloud interaction in summertime precipitating shallow cumulus over the Western North Atlantic” [Dataset]. *Zenodo*. <https://doi.org/10.5281/zenodo.8034149>
- Li, X.-Y., Brandenburg, A., Svensson, G., Haugen, N. E. L., Mehlig, B., & Rogachevskii, I. (2020). Condensational and collisional growth of cloud droplets in a turbulent environment. *Journal of the Atmospheric Sciences*, *77*(1), 337–353. <https://doi.org/10.1175/JAS-D-19-0107.1>
- Li, X.-Y., Wang, H., Chen, J., Endo, S., George, G., Cairns, B., et al. (2022). Large-eddy simulations of marine boundary layer clouds associated with cold-air outbreaks during the ACTIVATE campaign. Part I: Case setup and sensitivities to large-scale forcings. *Journal of the Atmospheric Sciences*, *79*(1), 73–100. <https://doi.org/10.1175/JAS-D-21-0123.1>
- Li, X.-Y., Wang, H., Chen, J., Endo, S., Kirschler, S., Voigt, C., et al. (2023). Large-eddy simulations of marine boundary-layer clouds associated with cold-air outbreaks during the ACTIVATE campaign. Part II: Aerosol–Meteorology–Cloud interaction. *Journal of the Atmospheric Sciences*, *80*(4), 1025–1045. <https://doi.org/10.1175/JAS-D-21-0324.1>
- Manshausen, P., Watson-Parris, D., Christensen, M. W., Jalkanen, J.-P., & Stier, P. (2022). Invisible ship tracks show large cloud sensitivity to aerosol. *Nature*, *610*(7930), 101–106. <https://doi.org/10.1038/s41586-022-05122-0>
- Moore, R. H., Wiggins, E. B., Ahern, A. T., Zimmerman, S., Montgomery, L., Campuzano Jost, P., et al. (2021). Sizing response of the Ultra-High Sensitivity Aerosol Spectrometer (UHSAS) and Laser Aerosol Spectrometer (LAS) to changes in submicron aerosol composition and refractive index. *Atmospheric Measurement Techniques*, *14*(6), 4517–4542. <https://doi.org/10.5194/amt-14-4517-2021>
- Morrison, H., Thompson, G., & Tatarskii, V. (2009). Impact of cloud microphysics on the development of trailing stratiform precipitation in a simulated squall line: Comparison of one- and two-moment schemes. *Monthly Weather Review*, *137*(3), 991–1007. <https://doi.org/10.1175/2008MWR2556.1>
- Painemal, D., Spangenberg, D., Smith, W. L., Jr., Minnis, P., Cairns, B., Moore, R. H., et al. (2021). Evaluation of satellite retrievals of liquid clouds from the GOES-13 imager and MODIS over the midlatitude North Atlantic during the NAAMES campaign. *Atmospheric Measurement Techniques*, *14*(10), 6633–6646. <https://doi.org/10.5194/amt-14-6633-2021>
- Painemal, D., & Zuidema, P. (2011). Assessment of MODIS cloud effective radius and optical thickness retrievals over the Southeast Pacific with VOCALS-REX in situ measurements. *Journal of Geophysical Research*, *116*(D24). <https://doi.org/10.1029/2011JD016155>
- Petters, M. D., & Kreidenweis, S. M. (2007). A single parameter representation of hygroscopic growth and cloud condensation nucleus activity. *Atmospheric Chemistry and Physics*, *7*(8), 1961–1971. <https://doi.org/10.5194/acp-7-1961-2007>
- Possner, A., Wang, H., Wood, R., Caldeira, K., & Ackerman, T. P. (2018). The efficacy of aerosol–cloud radiative perturbations from near-surface emissions in deep open-cell stratocumuli. *Atmospheric Chemistry and Physics*, *18*(23), 17475–17488. <https://doi.org/10.5194/acp-18-17475-2018>
- Radke, L. F., Hobbs, P. V., & Eltgroth, M. W. (1980). Scavenging of aerosol particles by precipitation. *Journal of Applied Meteorology*, *19*(6), 715–722. [https://doi.org/10.1175/1520-0450\(1980\)019<0715:SOAPBP>2.0.CO;2](https://doi.org/10.1175/1520-0450(1980)019<0715:SOAPBP>2.0.CO;2)
- Rauber, R. M., Stevens, B., Ochs, H. T., Knight, C., Albrecht, B. A., Blythe, A. M., et al. (2007). Rain in shallow cumulus over the ocean: The RICO campaign. *Bulletin of the American Meteorological Society*, *88*(12), 1912–1928. <https://doi.org/10.1175/BAMS-88-12-1912>
- Rémillard, J., & Tselioudis, G. (2015). Cloud regime variability over the azores and its application to climate model evaluation. *Journal of Climate*, *28*(24), 9707–9720. <https://doi.org/10.1175/JCLI-D-15-0066.1>
- Sandu, I., & Stevens, B. (2011). On the factors modulating the stratocumulus to cumulus transitions. *Journal of the Atmospheric Sciences*, *68*(9), 1865–1881. <https://doi.org/10.1175/2011JAS3614.1>
- Schlosser, J. S., Stammes, S., Burton, S. P., Cairns, B., Crosbie, E., Van Diedenhoven, B., et al. (2022). Polarimeter + lidar–derived aerosol particle number concentration. *Frontiers in Remote Sensing*, *3*. <https://doi.org/10.3389/frsen.2022.885332>
- Seinfeld, J. H., Bretherton, C., Carslaw, K. S., Coe, H., DeMott, P. J., Dunlea, E. J., et al. (2016). Improving our fundamental understanding of the role of aerosol? Cloud interactions in the climate system. *Proceedings of the National Academy of Sciences*, *113*(21), 5781–5790. <https://doi.org/10.1073/pnas.1514043113>
- Skamarock, W. C., Klemp, J. B., Dudhia, J., Gill, D. O., Liu, Z., Berner, J., et al. (2019). A description of the advanced research WRF model version 4. National Center for Atmospheric Research: Boulder, CO, USA [Software] (Vol. 145(145), p. 550). <https://doi.org/10.5065/1dfh-6p97>
- Smith, C. J., Kramer, R. J., Myhre, G., Alterskjær, K., Collins, W., Sima, A., et al. (2020). Effective radiative forcing and adjustments in CMIP6 models. *Atmospheric Chemistry and Physics*, *20*(16), 9591–9618. <https://doi.org/10.5194/acp-20-9591-2020>
- Sorooshian, A., Alexandrov, M. D., Bell, A. D., Bennett, R., Betito, G., Burton, S. P., et al. (2023). Spatially-coordinated airborne data and complementary products for aerosol, gas, cloud, and meteorological studies: The NASA ACTIVATE dataset. *Earth System Science Data*, *15*, 3419–3472. <https://doi.org/10.5194/essd-15-3419-2023>
- Sorooshian, A., Anderson, B., Bauer, S. E., Braun, R. A., Cairns, B., Crosbie, E., et al. (2019). Aerosol–cloud–meteorology interaction airborne field investigations: Using lessons learned from the U.S. West coast in the design of activate off the U.S. East Coast. *Bulletin of the American Meteorological Society*, *100*(8), 1511–1528. <https://doi.org/10.1175/BAMS-D-18-0100.1>
- Sorooshian, A., Feingold, G., Lebsock, M. D., Jiang, H., & Stephens, G. L. (2009). On the precipitation susceptibility of clouds to aerosol perturbations. *Geophysical Research Letters*, *36*(13). <https://doi.org/10.1029/2009GL038993>
- Team, A. S. (2020). Aerosol Cloud meTeorology Interactions oVer the western ATlantic Experiment [Dataset]. Retrieved from <https://asdc.larc.nasa.gov/project/ACTIVATE>
- Twomey, S. (1977). The influence of pollution on the shortwave albedo of clouds. *Journal of the Atmospheric Sciences*, *34*(7), 1149–1152. [https://doi.org/10.1175/1520-0469\(1977\)034<1149:TIOPOT>2.0.CO;2](https://doi.org/10.1175/1520-0469(1977)034<1149:TIOPOT>2.0.CO;2)
- Voigt, C., Schumann, U., Jurkat, T., Schäuble, D., Schlager, H., Petzold, A., et al. (2010). In-situ observations of young contrails – Overview and selected results from the CONCERT campaign. *Atmospheric Chemistry and Physics*, *10*(18), 9039–9056. <https://doi.org/10.5194/acp-10-9039-2010>

- Wang, H., & Feingold, G. (2009). Modeling mesoscale cellular structures and drizzle in marine stratocumulus. Part I: Impact of drizzle on the formation and evolution of open cells. *Journal of the Atmospheric Sciences*, 66(11), 3237–3256. <https://doi.org/10.1175/2009JAS3022.1>
- Wang, H., Rasch, P. J., & Feingold, G. (2011). Manipulating marine stratocumulus cloud amount and albedo: A process-modelling study of aerosol-cloud-precipitation interactions in response to injection of cloud condensation nuclei. *Atmospheric Chemistry and Physics*, 11(9), 4237–4249. <https://doi.org/10.5194/acp-11-4237-2011>
- Wang, H., Skamarock, W. C., & Feingold, G. (2009). Evaluation of scalar advection schemes in the advanced research WRF model using large-eddy simulations of aerosol–cloud interactions. *Monthly Weather Review*, 137(8), 2547–2558. <https://doi.org/10.1175/2009MWR2820.1>
- Wood, R., O. K.-T., Bretherton, C. S., Mohrmann, J., Albrecht, B. A., Zuidema, P., et al. (2018). Ultraclean layers and optically thin clouds in the stratocumulus-to-cumulus transition. Part I: Observations. *Journal of the Atmospheric Sciences*, 75(5), 1631–1652. <https://doi.org/10.1175/JAS-D-17-0213.1>
- Yamaguchi, T., Feingold, G., & Kazil, J. (2017). Stratocumulus to cumulus transition by drizzle. *Journal of Advances in Modeling Earth Systems*, 9(6), 2333–2349. <https://doi.org/10.1002/2017MS001104>
- Zhao, M., Golaz, J.-C., Held, I. M., Ramaswamy, V., Lin, S.-J., Ming, Y., et al. (2016). Uncertainty in model climate sensitivity traced to representations of cumulus precipitation microphysics. *Journal of Climate*, 29(2), 543–560. <https://doi.org/10.1175/JCLI-D-15-0191.1>